In-situ study of strontium segregation in $La_{0.6}Sr_{0.4}Co_{0.2}Fe_{0.8}O_{3-\delta}$ in ambient atmospheres using High-Temperature Environmental Scanning Electron Microscopy†

Mathew Niania,[a] Renaud Podor,[c] T. Ben Britton,[a] Cheng Li,[a] Samuel J. Cooper,[b] Nikolai Svetkov,[d] Stephen Skinner,[a] and John Kilner [a]

Samples of the Solid Oxide Fuel Cell cathode material $La_{0.6}Sr_{0.4}Co_{0.2}Fe_{0.8}O_{3-\delta}$ (LSCF) were annealed using High-Temperature Environmental Scanning Electron Microscopy (HT-ESEM) from room temperature to 1000 °C in atmospheres of pure oxygen, pure water and ambient lab air. Image series of each heat treatment were taken where microstructural changes were observed and compared between samples. Strontium segregation rate was found to be significantly increased in the presence of pure water as compared to pure O_2 and ambient air. Electron Backscattered Diffraction (EBSD) was performed in order to assess the effect of crystal orientation on particle formation and surface sensitive chemical analysis techniques were used to determine the chemical changes at the grain surface as a result of the different heat treatments. It was shown that crystal orientation affected the nature and growth rate of strontium-based particles, however, due to the pseduo-symmetry of $La_{0.6}Sr_{0.4}Co_{0.2}Fe_{0.8}O_{3-\delta}$, precise crystal orientation relationships could not be determined. The chemical composition of the grain surface was found to be approximately equal under each atmosphere.

1 Introduction

Intermediate Temperature Solid Oxide Fuel Cells (IT-SOFCs) are solid state devices that are used to efficiently convert chemical energy into electrical energy. They are part of a global strategy to reduce carbon emissions and provide a pathway to the use of hydrogen as an energy vector. Commonly used cathode materials are perovskite oxide Mixed Ionic-Electronic Conducting (MIEC) materials such as $La_{0.6}Sr_{0.4}Co_{0.2}Fe_{0.8}O_{3-\delta}$ (LSCF) due to their balance of ionic conductivity, electronic conductivity and chemical compatibility with adjacent components at intermediate operating temperatures. One of the primary issues with materials such as LSCF is their susceptibility to degradation processes causing a reduction in cell performance [1]. Generally, these processes cause surface passivation by the formation of insulating secondary phases at the surface, blocking catalytically active areas such as triple phase boundaries. Secondary phases are commonly formed by chemical reactions between the cathode material and gas stream components/impurities such as H_2O, silicon, sulphur and chromium [2–4]. However, 'A-site' cation segregation is also a significant cause of secondary phase growth at temperatures as low as 400 °C [5–7]. It has been shown that the aliovalent doping used to promote the functional properties inherently invokes A-site cation segregation to neutralise excess surface charge [8]. Given the prevalence of strontium as an A-site dopant this is often referred to as 'strontium segregation', although, it should be noted that similar behaviour is observed with different sized A-site dopants [9].

Gas stream composition and impurities influence cathode degradation, however, it has also been observed that gas-stream composition affects the oxygen reduction reaction as the dominant oxygen containing gas species (O_2, H_2O and CO_2) exchanging with the surface varies as a function of temperature [10]. It has been shown that the presence of water vapour in particular increases the oxygen exchange rate [11,12], however, it is not yet clear the role the gas stream has upon strontium segregation [13]. For materials such as LSCF the mechanical properties and their effect upon A-site segregation have been studied in much less detail. It has been shown that external stresses can affect the growth rate of strontium-based secondary phases [14], however, the precise cause for this alteration is not yet known. LSCF exhibits a domain like structure [15–17] as a result of shared Laue group symmetries found in the $R\bar{3}c$ space group, however, the effect this twinned

[a] Department of Materials, Imperial College London, London, SW7 2BP, UK
[b] Dyson School of Design Engineering, Imperial College London, London, SW7 2AZ
[c] ICSM, CEA, CNRS, ENSCM, Univ Montpellier, Marcoule, France
[d] Laboratory for Electrochemical Interfaces, Department of Nuclear Science and Engineering, Massachusetts Institute of Technology, 77 Massachusetts Avenue, Cambridge, Massachusetts 02139, United States

† Electronic Supplementary Information (ESI) available: [details of any supplementary information available should be included here]. See DOI: 10.1039/b000000x/

microstructure has upon strontium segregation is also unknown.

To date, strontium segregation in LSCF has primarily been observed post mortem or *ex-situ* (at room temperature in a high vacuum) due to the necessity of a high-vacuum in many common surface analysis techniques. However, it is clear that the gas composition and temperature has a direct effect on the processes occurring at the surface. This work aims to directly observe the segregation process in environments as close to SOFC operating conditions (*in-situ*) as possible. Using consistent samples, the underlying microstructure and its effect upon strontium segregation will also be directly compared between experiments.

2 Experimental

2.1 Sample Preparation

Samples of $La_{0.6}Sr_{0.4}Co_{0.2}Fe_{0.8}O_{3-\delta}$ (Praxair™* Specialty Ceramics powder) were uniaxially pressed at 2 tonnes of pressure in a 10 mm diameter die followed by an isostatic press at 300 MPa. Samples were then sintered at 1250 °C for 8 h using 300 °C/hour heating/cooling rates. Where required, samples were ground and polished using: silicon carbide papers (P800/P1200/P2400) followed by subsequent diamond suspensions (6,3,1,¼ μm). For samples to be analysed using EBSD an additional polishing step using colloidal silica (70% concentration in water) in a Buehler 'Vibromet 2' vibratory polisher was performed for 12 hours.

2.2 Electron Back-scattered Diffraction (EBSD)

Samples were analysed using a Zeiss Auriga FIB-SEM† with a Bruker 'e-Flash' EBSD detector using the settings found in Table 1. The location of the EBSD analysis was noted in order to be found later in the HT-ESEM. Prior to EBSD analysis forescattered electron (FSE) images were collected using Bruker's ARGUS™ imaging system. Contrast in FSE images is generated from the Electron Backscattered Pattern (EBSPs) and thus contains crystal orientation contrast. The Bruker eSpirit software was used to generate EBSD grain orientation maps and collected FSE images.

Table 1 EBSD settings

Setting	Value
Working Distance / mm	19.4
Beam Energy (keV)	20
Exposure Time (ms)	33
EBSD map area (μm)	60.4 × 45.3
Step Size (nm)	100
EBSP Resolution (px^2)	400 x 300

2.3 High-Temperature Environment Scanning Electron Microscopy (HT-ESEM)

A Quanta 200 ESEM FEG SEM (FEI Company‡) equipped with a 1500 °C heating stage was used to analyse samples under four different environments: 3 mbar research grade 99.999% high purity O_2, 3 mbar de-ionised H_2O (MilliQ system, 18.2 MOhms.cm) and 3 mbar ambient lab air (air temperature of 22 °C corresponding to a water vapour pressure of approximately 26 mbar p(H_2O)). In each environment samples were annealed from room temperature to 1000 °C with a 300 °C/hour heating rate followed by an isothermal anneal at the final temperature for between 1-2 hours. In order to measure the sample temperature accurately a separate thermocouple was used in the custom heating stage[18]. Images were recorded at regular intervals at 5,000x and 10,000x magnification for the duration of the experiment. Compiled videos of each image series may be found in the supplementary material of this paper. Backscattered electron (BSE) and Energy Dispersive X-Ray (EDX) spectra were taken after the H_2O experiment. To achieve this, the sample had to be cooled down to room temperature and exposed to ambient air in order to replace the detectors and to adjust the working distance.

During the experiments performed under a gaseous atmosphere, the electron signal was collected using a dedicated high temperature gaseous secondary electron detector[19]. Using this detector, the information is restricted to the sample topography. Above a certain partial pressure the signal to noise ratio restricts the ability to focus the electron beam. For this equipment the upper limit for high quality imaging was approximately 3 mbar.

2.4 Image Analysis

The image series were aligned using linear stack alignment[20] and cropped to remove significant whitespace create by image rotation. Trainable Weka Segmentation[21] was used to create binary threshold images for use with the standard particle analysis algorithms in ImageJ[22]. This method was found to be superior to the standard default Canny-Deriche edge detection method[23] due to the complexity of the microstructures observed in this experiment.

2.5 Auger Electron Spectroscopy

A Physical Electronics Model 700§ scanning nanoprobe Auger electron spectroscopy (AES) instrument was used to observe cation composition in both the particles and exposed grain surface. Electron beam settings of 20 keV and 10 nA were used for both SEM imaging and the Auger electron excitation. The La MNN, Sr LMM, Fe LMM, and Co LMM Auger emissions were measured for quantifying the surface cation composition. Smoothing and differentiation of the AES spectra collected were carried out using the Savitsky-Golay algorithm. Quantification of the AES differential spectra was performed using peak-to-peak intensities of the tight-scans of the noted emissions from the constituent cations. The probing depths (3xIMFP) are about 8.0 nm for Sr LMM, 4.0 nm for La MNN, 4.5 nm for Co LMM and 4.3 nm for Fe LMM emissions. Standard sensitivity factors were used for the chemical quantification with AES (Physical Electronics Inc., 2006), however, the actual sensitivity factors for these emissions may vary from the provided standards. Therefore, rather than the absolute values of the surface chemical content, consistent

* ,Praxair, 10 Riverview Dr., Danbury, CT, 06810, USA

† Carl-Zeiss-Straße 22, 73447, Oberkochen, Germany

‡ FEI Company, 5350 NE Dawson Creek Drive, Hillsboro, Oregon, 97124 USA

§ Physical Electronics, 18725 Lake Drive East, Chanhassen, MN, 55317

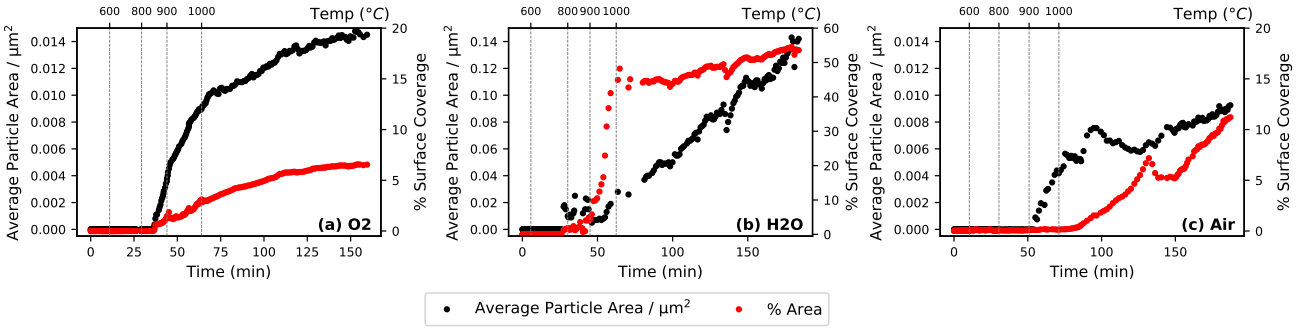


Fig. 1 Average particle area and percent surface coverage with respect to time and temperature for an LSCF sample annealed in (a) 3 mbar oxygen, (b) 3 mbar H_2O and (c) 3 mbar ambient lab air. It should be noted that the scales are equal in (a) and (c), however, in (b) average particle area is 10x that of the others and surface coverage 3x that of the others.

qualitative trends may be observed between samples of the same material.

2.6 Low Energy Ion Scattering

To probe the outermost atomic layer of the surface, samples were also analysed using Qtac 100 (ION-TOF[¶]) Low Energy Ion Scattering (LEIS) [24]. Samples were analysed using 3 keV Helium primary beam to provide an 'overview' of the surface. This was then followed by analysis using a 5 keV Neon primary beam to separate the cation peaks and allow determination of surface composition. LEIS depth profiles were also performed in conjunction with 5 keV Neon analysis. The sputter beam used was a 1 keV $^{40}Ar^+$ sputter beam with a raster area of 1.5 x 1.5 mm. Depth profiles were run until the composition reached constant stoichiometry.

3 Results

In-situ HT-ESEM experiments were performed in atmospheres of O_2, H_2O and ambient air. Secondary electron images at 5,000x and 10,000x magnification were collected during the heating phase and isotherm to directly observe microstructural modifications induced by the anneal regime. Particle counts and percent surface coverage for each environment may be seen in Figure 1. Backscattered electron images were collected post-anneal and correlated with AES elemental maps to characterise the chemical nature of any observed degradation features. LEIS surface spectra were collected to quantify cation ratios of the outermost atomic layer and LEIS depth profiles were performed to study changes occurring at the sub-surface.

3.1 High Temperature Environmental Scanning Electron Microscopy

3.1.1 HT-ESEM: High Purity Oxygen

Figure 2 shows selection of images representative of the different steps of precipitate formation and growth during the heating phase and 1000 °C isotherm under 3 mbar O_2. See supplementary Video 1 and 2 for high resolution videos at 5,000x and 10,000x magnification respectively. The average particle area and percentage surface coverage may be seen in Figure 1(a). It should be noted that the concentration of water vapour in this gas was less than 1 part per million.

Initially no obvious changes to the grain surface was observed, however, at 850 °C thermal etching of the grain boundaries followed by the onset of wide spread particle growth is seen. Particle growth is rapid between 850-1000 °C, but begins to slow during the 1000 °C isotherm as a result of Ostwald ripening processes.

As can be seen in Figure 2, much of the growth begins on the grain boundaries, however, growth may also be seen to follow mechanical damage induced during polishing (scratches). However, as also observed by Oh *et al.* [5], there is significant nucleation within the grain body. The onset of particle growth and particle growth rate appears homogeneous across all grains. Particle shape varies, with some appearing rod-like, rounded or showing evidence of a faceted rectangular/pyramidal shape, however, there is no apparent consistency in particle shape between grains.

3.1.2 HT-ESEM: Pure H_2O

Figure 3 shows selection of images representative of the different steps of precipitate formation and growth during the heating phase and 1000 °C isotherm under 3 mbar pure H_2O. See supplementary Video 3 and 4 for high resolution videos at 5,000x and 10,000x magnification respectively.

Similar to observations in oxygen, secondary phase particle growth is seen, however, the rate and quantity of particle growth far exceeds that of oxygen. The average particle area and percentage surface coverage determined from the image series is reported in Figure 1(b). In this sample no particle growth was observed prior to the thermal etching of the grain boundaries. The onset of particle formation was observed at 825 °C, again nucleating predominantly on the grain boundaries but also in the grain body. At approximately 960 °C particles are seen to agglomerate rapidly and continue to agglomerate during the 1000 °C isotherm. At the end of the experiment, particles several microns along their largest dimension can be observed across the whole surface of the sample.

Due to the considerable number of particles formed in this environment it is possible to observe different growth patterns at the grain surface. As can be seen in Figure 3(g) four different growth patterns are observed for the grains marked A-D (a high

¶ IONTOF GmbH, Heisenbergstraße 15, 48149, Münster

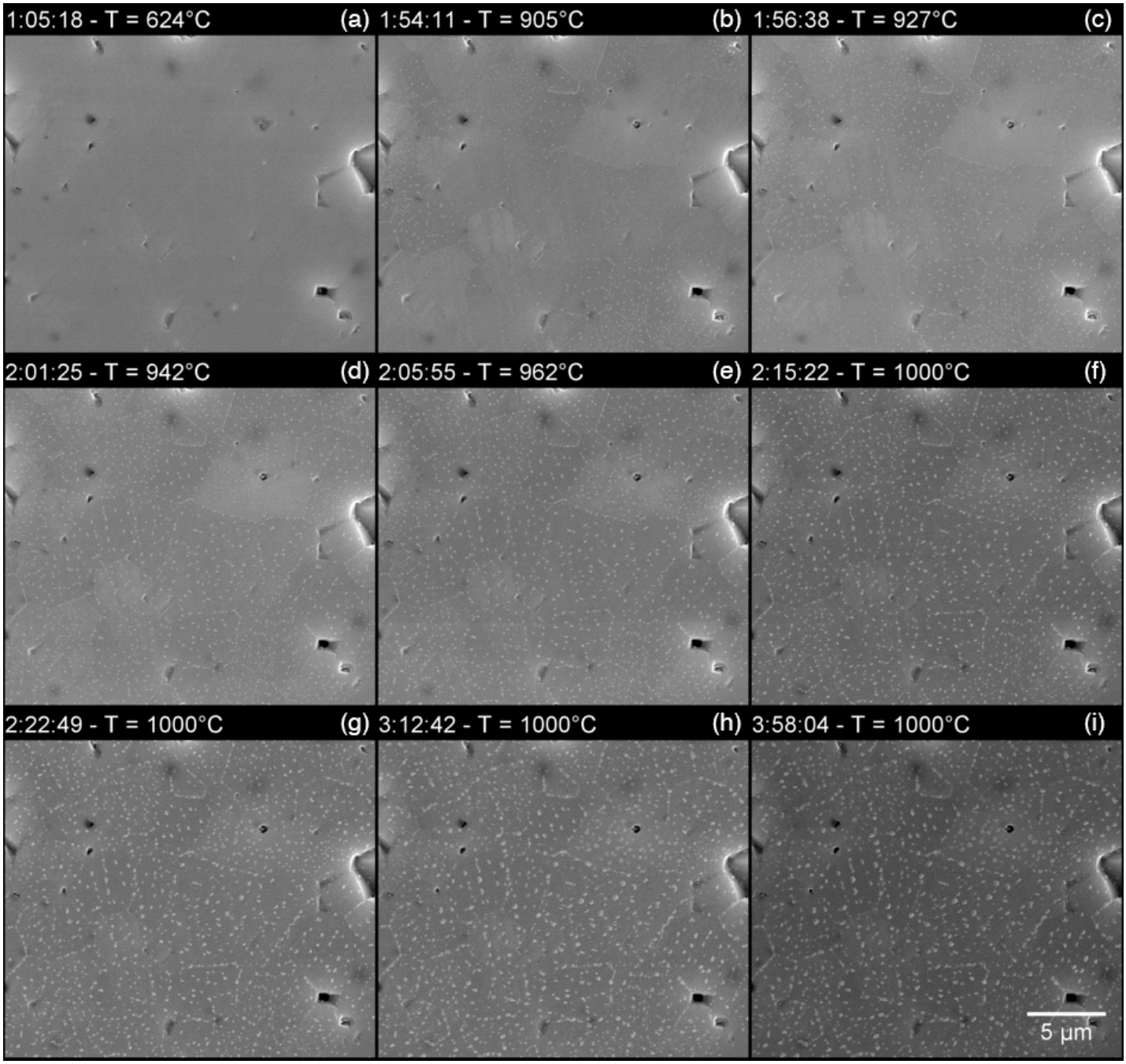


Fig. 2 HT-ESEM micrograph series of the LSCF sample annealed in 3 mbar O_2 where (a - e) shows particle growth during the heating phase and (f - i) shows particle growth during the 1000 °C isotherm.

resolution image of this panel is included in the supplementary information). The fraction of each grain type was calculated by correlating the HT-ESEM image with EBSD grain orientation map.

Grain A: Pyramidal shaped particles orientated in the same direction. Nucleation and agglomeration of the particles appears to follow equidistant parallel lines. Similar particles also found at the grain boundaries. Fraction of grain type A: 14%.

Grain B: Rod-shaped particles orientated in the same direction. Nucleation and agglomeration of the particles appears to follow equidistant parallel lines, however, they appear closer together than in grain A. Fraction of grain type B: 13 %.

Grain C: Homogeneous growth across the whole grain with no apparent relationship to the grain surface. A small denuded area adjacent to the grain boundary. Fraction of grain type C: 21%.

Grain D: Homogeneous growth across the whole grain surface, where the average particle size appears greater than in grain type C. Much larger denuded area adjacent

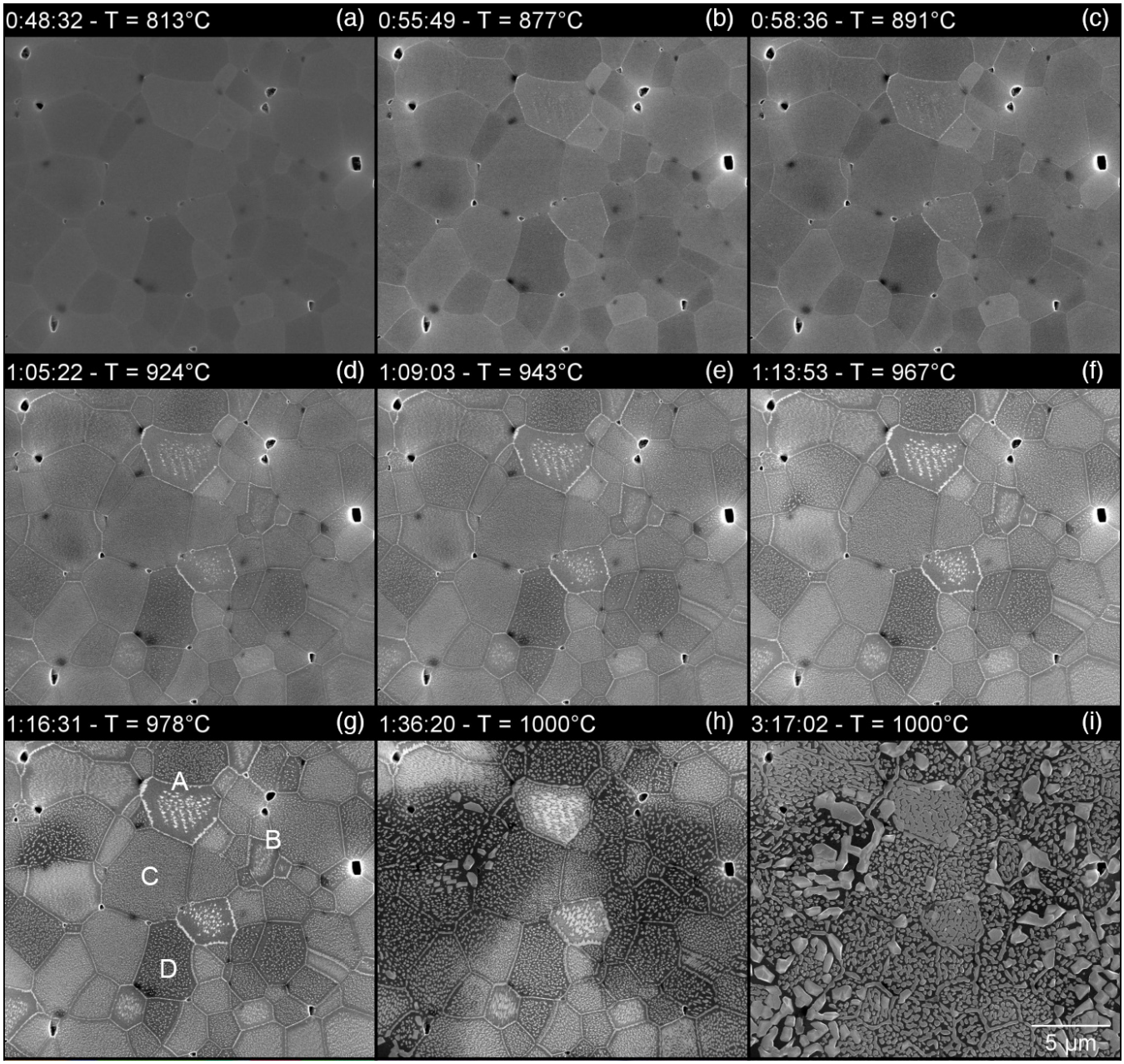


Fig. 3 HT-ESEM micrograph series of the LSCF sample annealed in 3 mbar H_2O where (a - g) shows particle growth during the heating phase and (h - i) shows particle growth during the 1000 °C isotherm. Individual grains discussed in the text have been labeled A - D in panel (g). A high resolution image of this panel is included in the supplementary information.

to the grain boundary. Fraction of grain type D: 52%.

Due to the consistent shape, orientation and prevalent growth direction of the particles in grain type A and B it would appear that particle growth is epitaxial within these grains. Whereas particle growth appears more homogeneous in grain type C and D suggesting no apparent correlation with the underlying microstructure. Figure 4 shows the individual particle growth rate of each grain. The onset of particle growth, agglomeration rate (seen by the slope of the average particle area), final surface coverage and final average particle area appears consistent between grain B, C and D despite the clear differences in particle shape. Grain A, however, shows a faster agglomeration rate and higher overall surface coverage prior to agglomeration.

Additionally, it may be seen that immediately surrounding the grain boundaries there is a denuded region devoid of any particles. Oh *et al.*[5] observed a similar effect, however, did not comment upon it. For grains with a homogeneous growth pattern (grains C and D) the denuded region without particles may be seen to be 150±25 nm in width. For grains exhibiting directional triangular/rod shaped growth (grain A and B) the region is 350±25 nm in diameter. Particle size appears to increase with the denuded width, implying that Ostwald ripening is occurring at particles within the grain and at the grain boundaries, albeit at different rates between different grains.

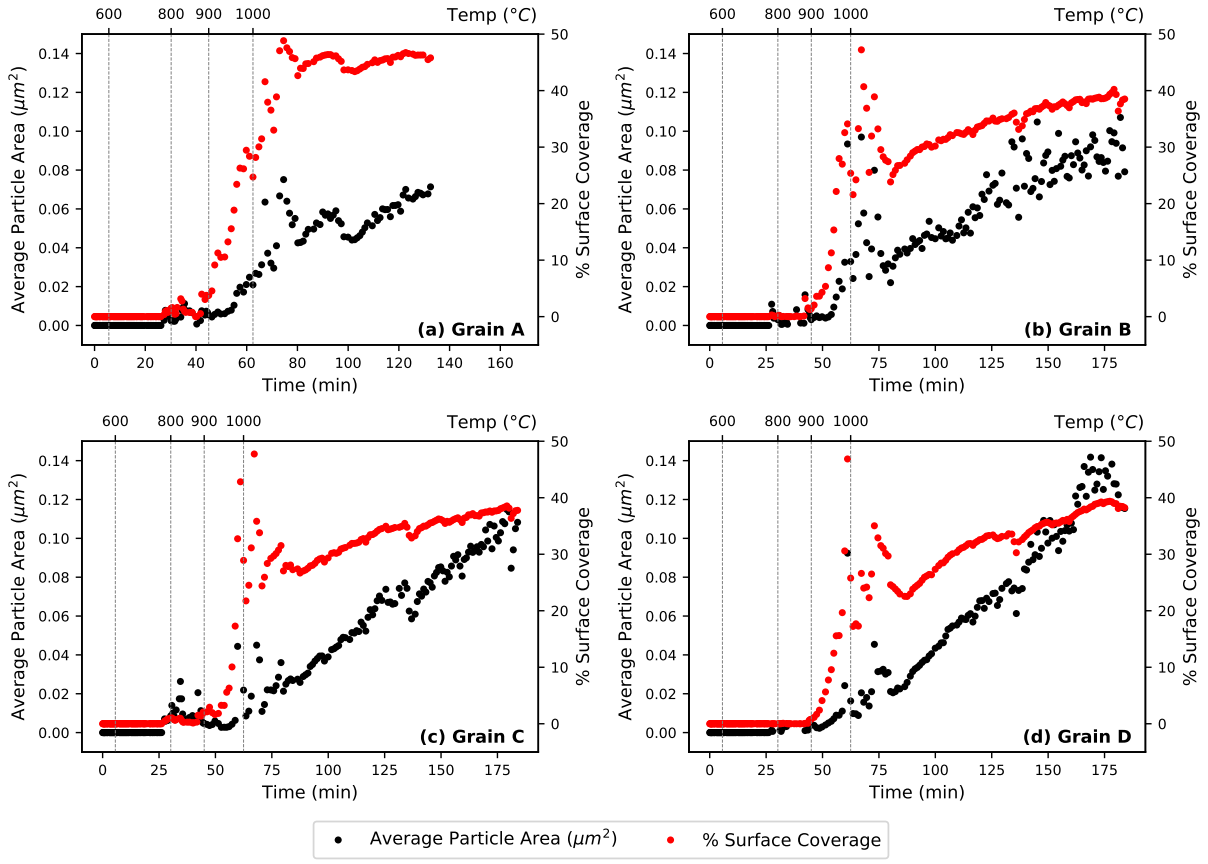


Fig. 4 Average particle area and percent surface coverage with respect to time and temperature for an LSCF sample annealed in H_2O showing the growth rate for grain A, B, C and D. The scale for both Y-axes is equal on each plot. In grain A particles were seen to agglomerate into a large connected particle network after 120 minutes, reducing the accuracy of the particle analysis methodology significantly. This has been removed for clarity.

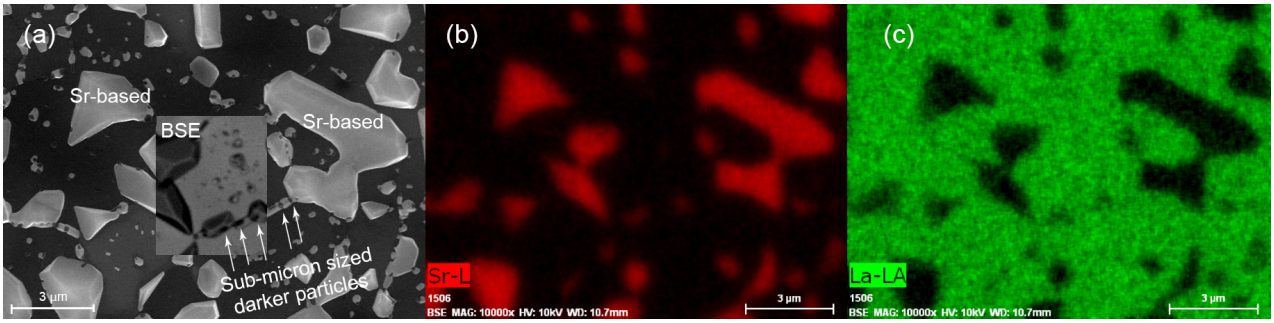


Fig. 5 Very large particles observed after an hour of isothermal annealing at 1000 °C in H_2O showing (a) the secondary electron image overlaid with a BSE image of the same area, (b) corresponding Sr (Lα line) EDX elemental map and (C) corresponding La (Lα line) EDX elemental map, both recorded at 10 kV.

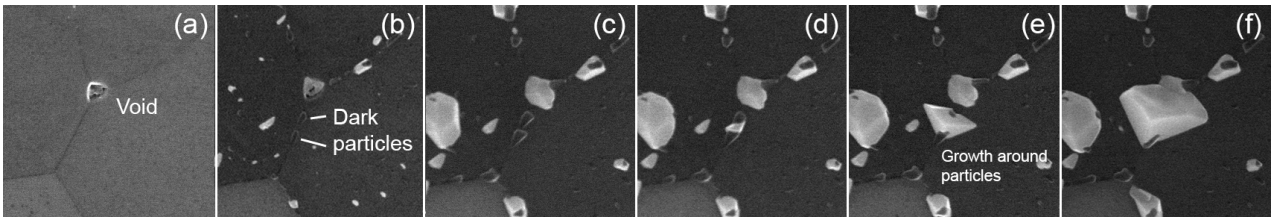


Fig. 6 Image series showing the growth of smaller, darker particles before the growth and agglomeration of larger Sr-based particles for the sample annealed in H_2O.

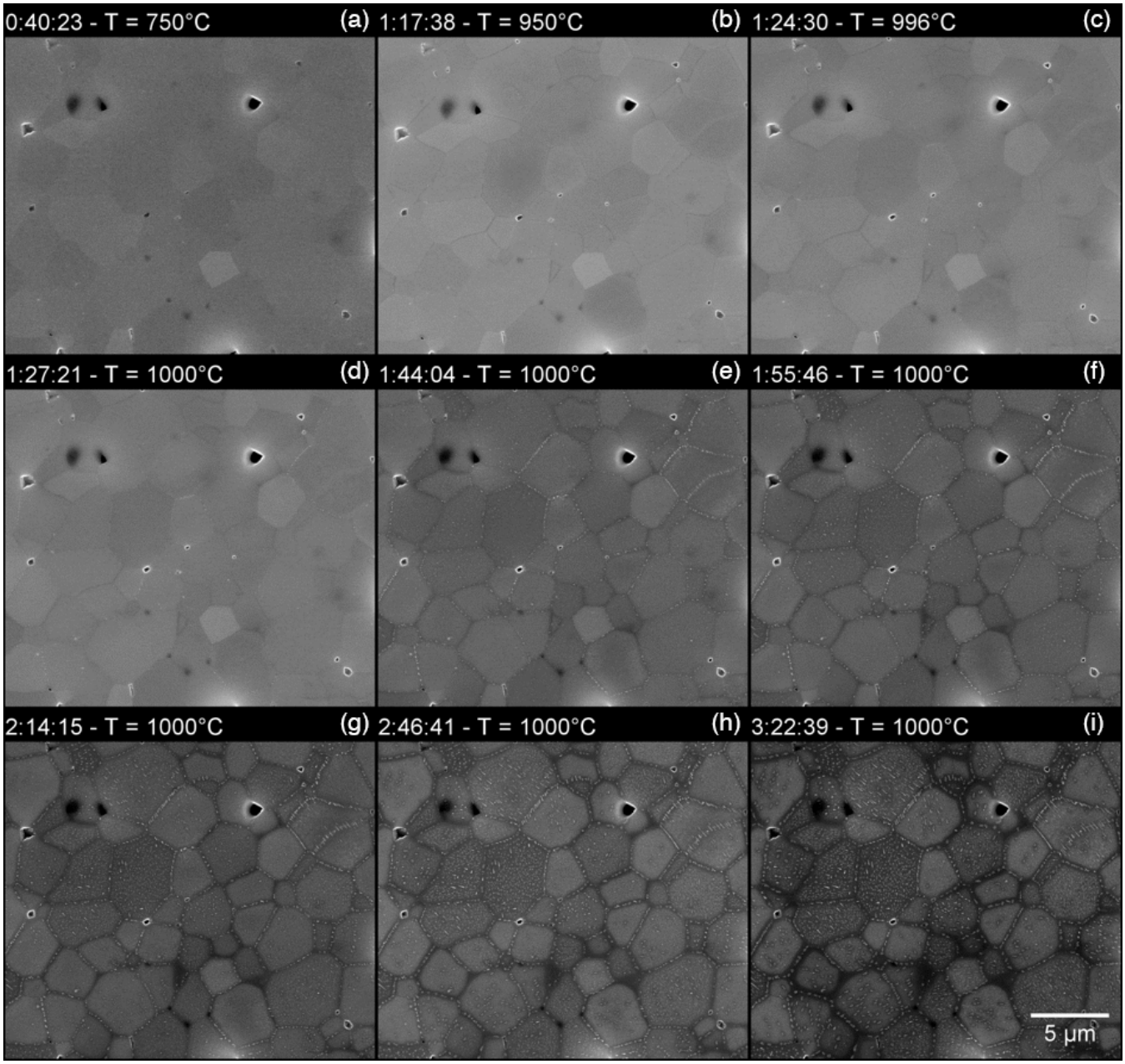


Fig. 7 HT-ESEM micrograph of the LSCF sample annealed in ambient lab air where (a - c) shows particle growth during the heating phase and (d - i) shows particle growth during the 1000 °C isotherm.

As can be seen in Figure 5, after approximately one hour of the 1000 °C isothermal anneal, particles several microns along their largest dimension had formed across the whole material surface. In certain locations smaller, sub-micron sized, darker particles could be observed. From Figure 5(a) it can be seen that the smaller particles are still present in the BSE image suggesting a compositional difference between the two particles. Observing Figure 6 (and Videos 3 and 4 in the supplementary material) the smaller, darker particles appear to grow first, predominantly on grain boundaries, then the larger, lighter particles appear to grow around them. Figure 5(b) shows that the large particles are predominantly strontium-based (and conversely Figure 5(c) shows an inverse relationship to Lanthanum). However, the spatial resolution of the EDX imaging was insufficient to identify the composition of smaller particles.

3.1.3 HT-ESEM: Ambient Lab Air

Figure 7 shows selection of images representative of the different steps of precipitate formation and growth during the heating phase and 1000 °C isotherm under 3 mbar ambient lab air. See supplementary Video 5 and 6 for high resolution videos at 5,000x and 10,000x magnification respectively. The average particle area and percentage surface coverage may be seen in Figure 1(c).

Similar to observations seen in pure O_2, particle growth is initially rapid but begins to slow during the 1000 °C isotherm. However, the onset of particle growth is not seen to start until approx-

Table 2 Table of values corresponding to the AES spot analysis seen in Figure 8.

Location	Atmosphere	La (At. %)	Sr (At. %)	Co (At. %)	Fe (At. %)
Grain	O_2	17.1	75.3	1.4	6.2
	H_2O	17.0	74.8	1.1	7.1
	Air	19.3	71.3	1.8	7.6
Particle	O_2	7.90	88.5	1.0	2.6
	H_2O	5.50	92.2	0.2	2.1
	Air	8.6	87.6	0.7	3.1

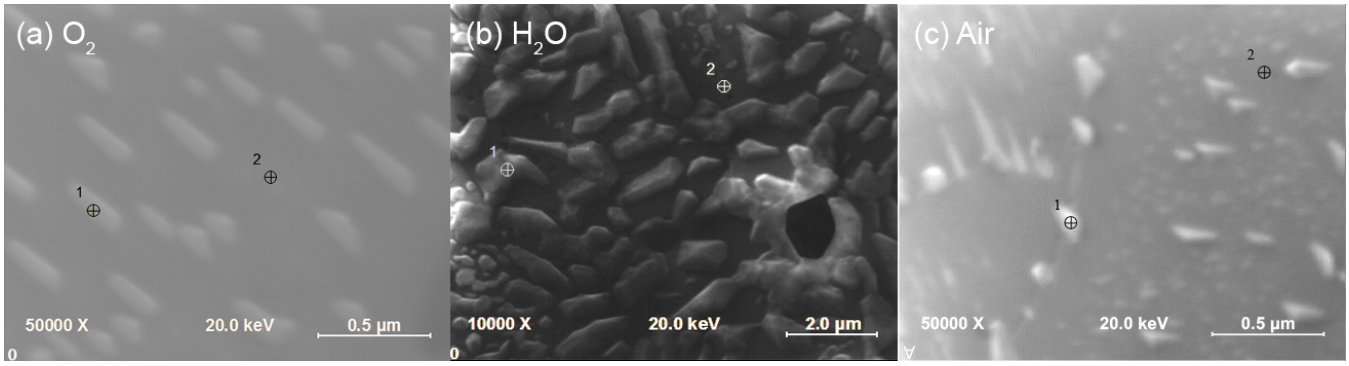


Fig. 8 Secondary electron images of each AES analysis area for (a) oxygen, (b) water and (c) ambient air. Point 1 shows the anlaysis spot for a 'particle' and point 2 the analysis spot of an 'unsegregated' grain surface in each atmosphere.

imately 1000 °C. Particle growth also begins on the grain boundaries followed by within the grain body. For the grains in which particles grew, the majority of the particles are aligned along a prevalent direction. However, a minority of the particles are either rounded or grew orthogonally to the prevalent direction.

At the end of the experiment a significant change in contrast may be seen in the surface of some grains. The spatial and chemical resolution of the experiment was insufficient to determine if this was due to particle growth, or a morphological change to the grain surface as a result of chemical corrosion due the presence of CO_2 [25].

3.2 Electron Backscattered Diffraction

One common observation in the HT-ESEM data is that the surface microstructure appears to influence particle growth. Grain boundaries and topographical features (microstructural and induced during polishing) are seen to act as heterogeneous nucleation sites for particles, however, unusually, in each experiment particle growth is observed within the body of seemingly featureless polished grain surfaces.

Crystallographic studies of LSCF have primarily focussed upon the response to changes in temperature and $p(O_2)$ [26,27]. More recently the ferroelastic properties are beginning to be studied as it appears that they can influence both the mechanical and chemical properties [16,28]. Of particular interest is the presence of the ferroelastic domains (or 'twin systems') seen in LSCF [17] resulting from the low symmetry of the rhombohedral ($R\bar{3}c$) crystal system. An additional consequence of this crystal structure is the presence of 'pseudo-symmetry' causing misinterpretation (or 'misindexing') of grain orientation by the EBSD software [29]. As can be seen in Figure 9(a), twin systems were directly observed in this work, however, as shown in Figure 9(b) multiple possible solutions were found within the same grain as a result of the pseudo-symmetry, making interpretation of the EBSD data difficult.

Without the ability to counteract uncertainty due to pseudo-symmetry it was not possible to define absolute grain orientation or the twin structure. A qualitative approach was taken to show grains with similar orientation. LSCF 6428's trigonal crystal structure, $R\bar{3}c$, may be related to the Pm3m space group by octahedral tiling, as described by Glazer [30], because the two structures share the same cation-linkage network. As a result the a- and b-axes may be equated, but the c-axis is smaller than the actual cell height. Thus, it is possible to show which grains have an equivalent orientation, however, the absolute grain orientation cannot be determined. For example, in Figure 9(c) and Figure 10 each grain colour represents a different grain orientation and is equivalent for grains of the same colour. As can seen in Figure 10 it is noticeable that particle density for similarly orientated grains is consistent across the observed area: grain type A always appears a dark blue, grain type B a light blue, grain type C red and grain type D green. Purple and yellow grains share similar behavior to grain type D.

3.3 Auger Electron Spectroscopy

AES was performed to characterise individual particles, as well as the grain composition, after the heat treatments. Figure 8 shows spot analysis positions for samples annealed in oxygen and water where spot (1) refers to a particle and spot (2) the grain surface. Table 2 shows the relative elemental composition for each point. As can be seen, the composition of the particles is predominantly strontium based, however, other elements are detected as the information depth for Auger analysis extends several nm below the immediate surface. The composition of the particles is approximately equal in each atmosphere but particles annealed in water

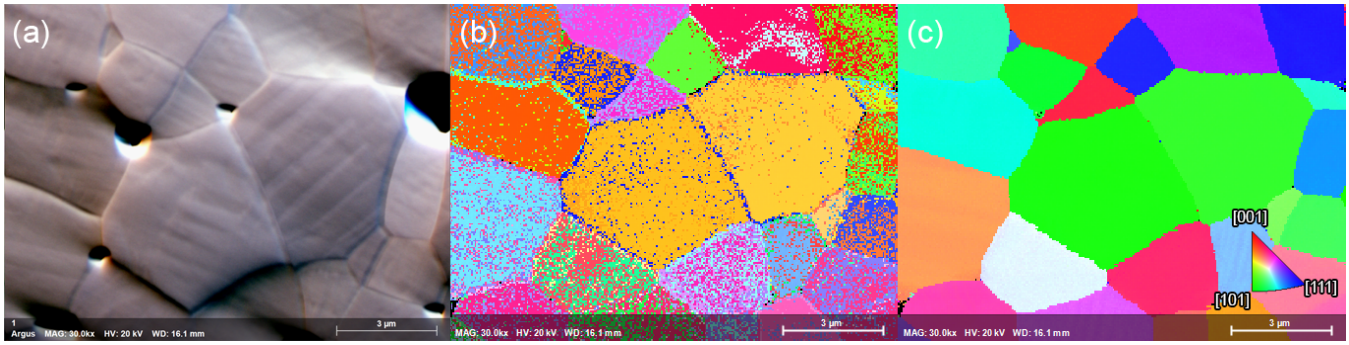


Fig. 9 Showing (a) the Argus FSE image of LSCF and the twinning structure, (b) the EBSD grain orientation map indexed using the $R\bar{3}c$ crystal structure and (c) indexed using the Pm3m crystal structure.

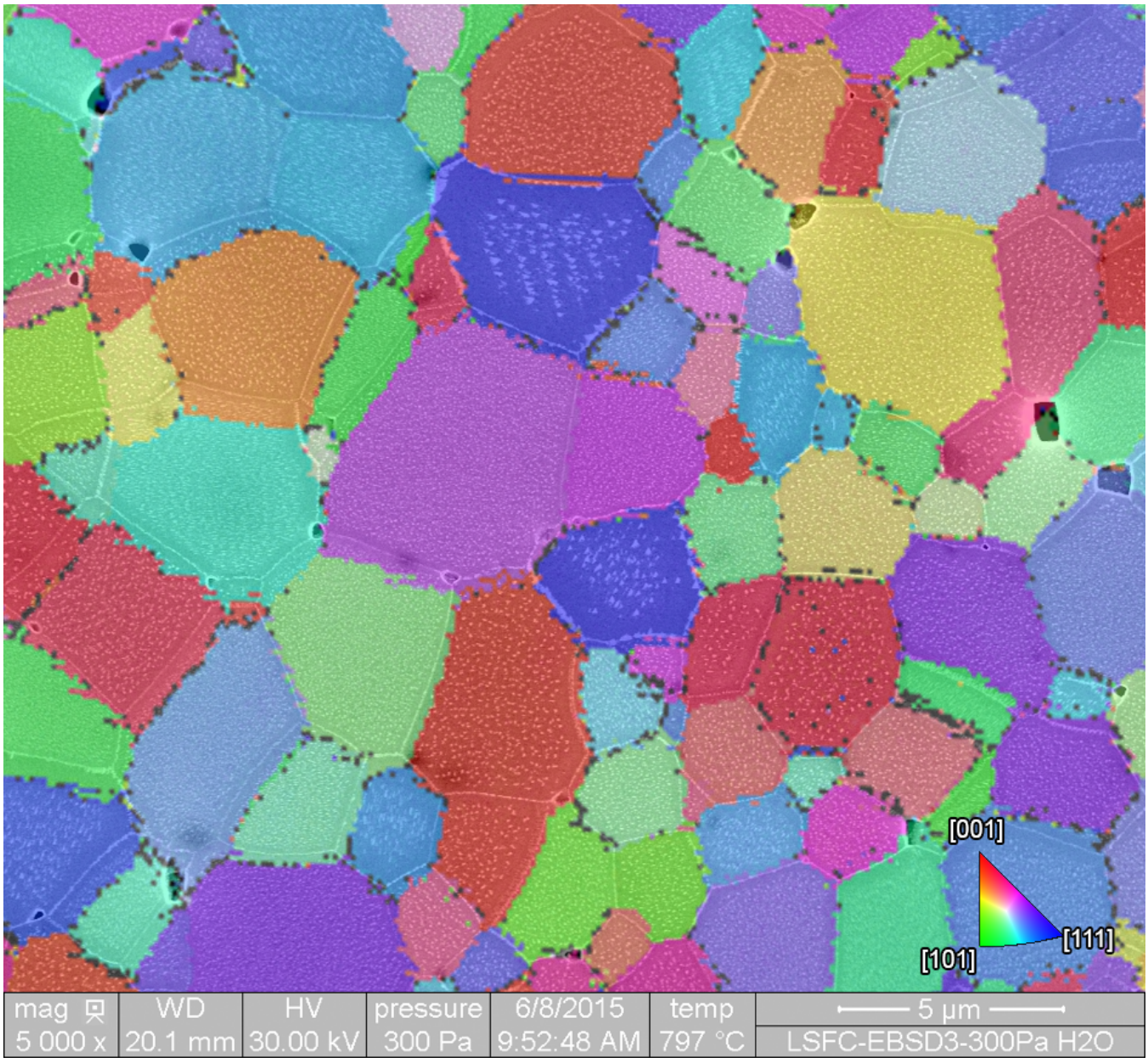


Fig. 10 Showing the EBSD grain orientation map indexed using the Pm3m crystal structured overlaid over an HT-ESEM micrograph from the H2O anneal. The micrograph shows particle growth prior to agglomeration as it more clearly shows the difference between the particles between grains.

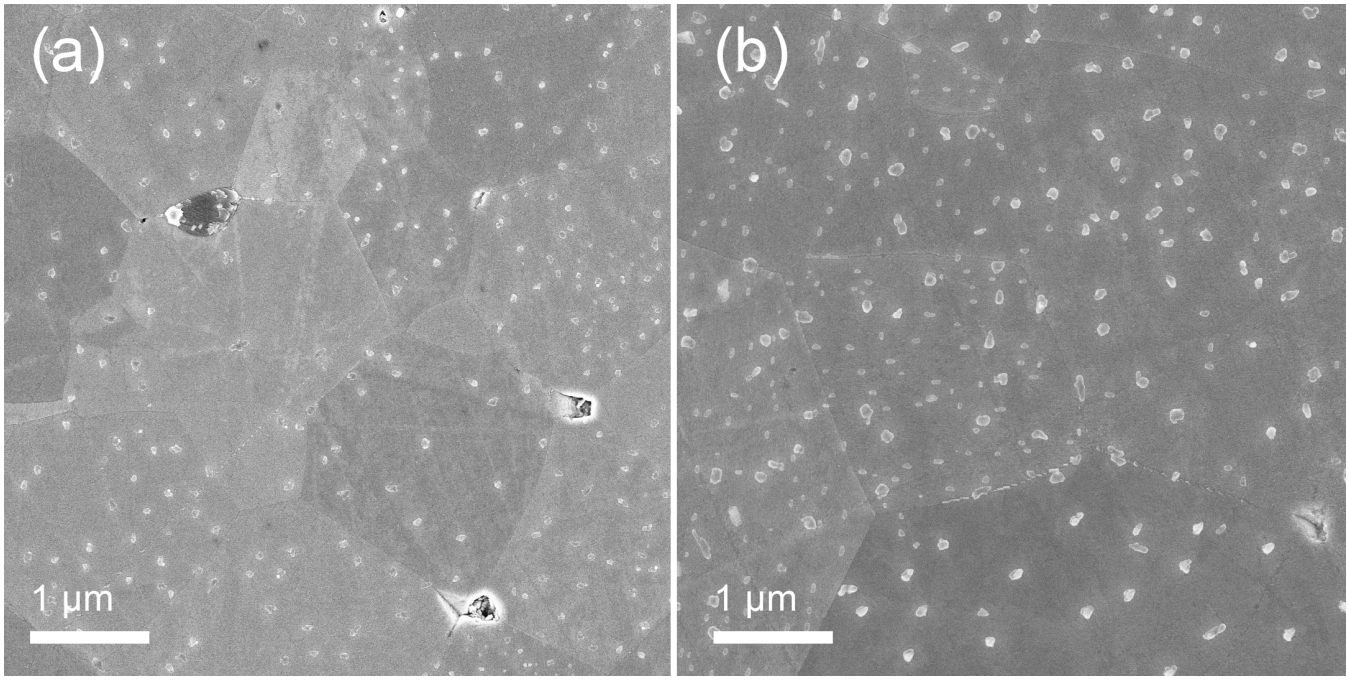


Fig. 11 Showing micrographs of LSCF samples (a) annealed at 650 °C in pure oxygen and (b) annealed at 650 °C in pure oxygen followed by a 45 minute anneal in ambient air. Collected using a LEO Gemini 1525 FEG-SEM.

display a greater strontium content. However, as the particles are larger, there will be reduced electron beam interaction in the bulk. Interestingly, the composition of the grain surface for each sample is approximately equal.

3.4 Low Energy Ion Scattering

Surface LEIS spectra were collected to analyse surface composition of the material post anneal. LEIS depth profiles were used to study the immediate sub-surface (5-6 nm in depth). LEIS is a highly surface sensitive technique probing the outermost atomic layer[24], however, in contrast to AES, it has a relatively low lateral resolution (analysis area ranging from 500-1500 μm^2). Due to the sensitivity of the technique, strict control of sample preparation was required and as such a separate set of LSCF samples were required. The localised, differentially pumped, low partial pressure environment found in the HT-ESEM could not be recreated for these samples so conditions relevant to the isotopic exchange and back-exchange techniques[12,31] were used instead. Samples were annealed at 650 °C for 14 hours in 200 mbar 99.999% pure oxygen. One sample was then annealed in an atmosphere of 1 bar ambient lab air for an additional 45 minutes, analogous to a back-exchanged sample. It should be noted the thermal history of these samples is different to the HT-ESEM samples; however, as can be seen in Figure 11(a) and (b), the average particle area was found to be 0.01 μm^2 and percent surface coverage approximately 8% for both samples. These values are very similar to that observed in the HT-ESEM (see Figure 1(a) and (c)) so it is suggested that despite the differences in thermal history the surface of the HT-ESEM and LEIS samples are comparable.

Figure 12(a) shows LSCF surface spectra taken using a 3 keV helium primary ion beam for both samples. The vertical dashed lines show the onset scattering energy of each surface atom. These are followed by scattering peaks for each element. Using helium as a primary ion it can be seen that peak separation is poor between lanthanum and strontium. Additionally, cobalt and iron have very similar masses and as such their scattering peaks overlap completely. This makes quantification of LSCF cation ratios difficult using a helium primary, however, the purpose of using helium was to 'survey' the surface and assess the cleanliness of the sample. If the sample contained significant surface contamination then the scattering peaks of interest will be attenuated by an unknown factor, thus causing systematic errors. A large degree of contamination often results in a substantial loss of signal. Small peaks were detected for sodium, magnesium and potassium (or calcium), however, the peaks for the main constituent atoms are still well defined, thus the samples were considered to be sufficiently clean.

Table 3 Cation ratio at the surface for LSCF samples annealed in pure oxygen and ambient air.

Atmosphere	La (At. %)	Sr (At. %)	Co (At. %)	Fe (At. %)
O_2	18 ± 1	60 ± 1	5 ± 1	17 ± 1
Ambient Air	2 ± 1	91 ± 1	1 ± 1	6 ± 1

Even from the helium spectra it is clear that, from the sample with the supplementary anneal in ambient air, there is a significantly greater concentration of strontium at the surface. This observation is consistent with Druce *et al.*[6] whereby there is almost complete depletion of lanthanum, cobalt and iron at the surface. In order to quantify this effect, 5 keV neon spectra were collected. Neon provides much better resolution for the heavier elements but cannot be used for the common contaminants such

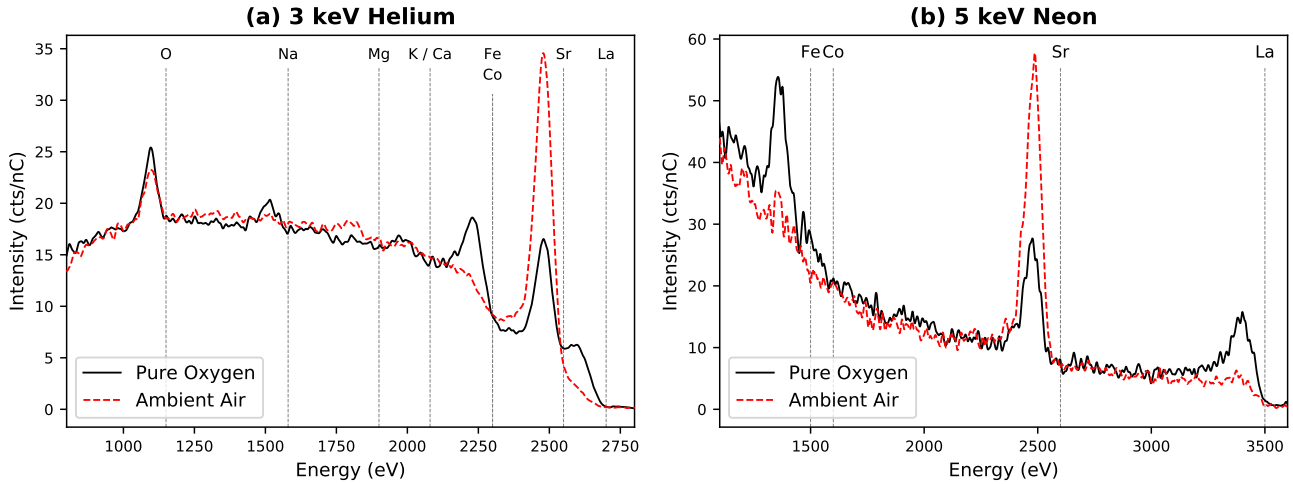


Fig. 12 LEIS spectra for LSCF samples annealed in pure oxygen and ambient air using (a) 3 keV Helium primary beam and (b) 5 keV Neon primary beam.

as Na, hence the use of He survey spectra as a starting point. Figure 12(b) shows surface spectra of LSCF samples annealed in oxygen and ambient air. LEIS spectra are plots of scattering intensity against selected energy, therefore the area under the peak represents the number of ions scattered by an element. Surface Lab 6 software (ION-TOF[||]) was used to fit this data and the resulting surface cation ratios are shown in Table 3.

The LEIS data can be strongly influenced by the presence of particles on the surface. The LEIS beam spot size is on the order of tens of microns, meaning that a LEIS spectrum represents the average composition across the surface (individual particles cannot be resolved). Topographical effects will cause attenuation of the scattered signal, however, the presence of particles will prevent the surface from being probed as a result of direct coverage and shadowing effects of the beam[24]. Therefore, any enhanced strontium signal must be a combination of the outer surface of the strontium particles and the exposed (but modified) grain surfaces. Again, the sample with the supplementary ambient air anneal displays a higher concentration of strontium with a respective decrease in the other elements. The sample annealed in pure oxygen also exhibits an enhanced surface strontium content, however, the absolute value is lower. The *ex-situ* SEM analysis of the LEIS samples suggests that the percentage of the surface covered by particles was approximately 8% for both samples. The enhancement in the Sr signal is greater than this value, thus the majority of surface strontium must exist on the grain surface.

From this experiment we can see that the supplementary anneal in air has had a dramatic effect upon the surface Sr content over the O_2-only anneal. This implies that either the H_2O or the CO_2 has a large effect upon the segregation. As the $p(O_2)$ and temperature are kept constant, this implies that there is an extra driving force for Sr segregation when these components are present in the gas phase.

[||] IONTOF GmbH, Heisenbergstraße 15, 48149, Münster

3.4.1 LEIS Depth Profiles

Figure 13 shows LEIS depth profiles (5 keV Ne) of the samples annealed in pure oxygen and with the supplementary ambient air anneal. Samples were sputtered until cation counts became constant. It was assumed that at this point that the bulk cation stoichiometry had been reached (i.e. neglecting preferential sputtering) and the cation ratio at any point of the depth profile could be calculated relative to the bulk value. Due to very short sputter depths (a few nanometers), sputter depth has been estimated based upon the sputter rate of LSCF and the ion dose.

As can be seen from both profiles, the surface and immediate sub-surface is enhanced in strontium and deficient in lanthanum over approximately 0.5 nm of depth. In both samples it may be seen that the concentration of Co is enhanced and the Fe is depleted over the first few nanometers, however, for the sample with the supplementary anneal in ambient air there is an increase of Fe and corresponding decrease of Co at the immediate surface. It would appear that the concentration of B-site cations are linked, however, care should be taken when interpreting this result. Each sputter step induces 'mixing' as a result of ballistic effects. The region affected by mixing is dependent upon the ion beam energy and incident angle. As such, during a depth profile, slight changes seen in the integrated cation ratios may contain this error.

4 Discussion

It has been shown that particle growth occurs in each of the tested environments. Consistent with the literature, growth is also seen at lower temperatures if the anneal time is increased[6]. As can be seen from Figure 14 the gas composition has a clear effect upon particle growth and particle morphology. A common observation between environments is the onset of growth on the grain boundaries, followed by growth within the body of the grains. Grain boundaries are often preferential sites for heterogeneous nucleation, however, growth within the body of grains is more

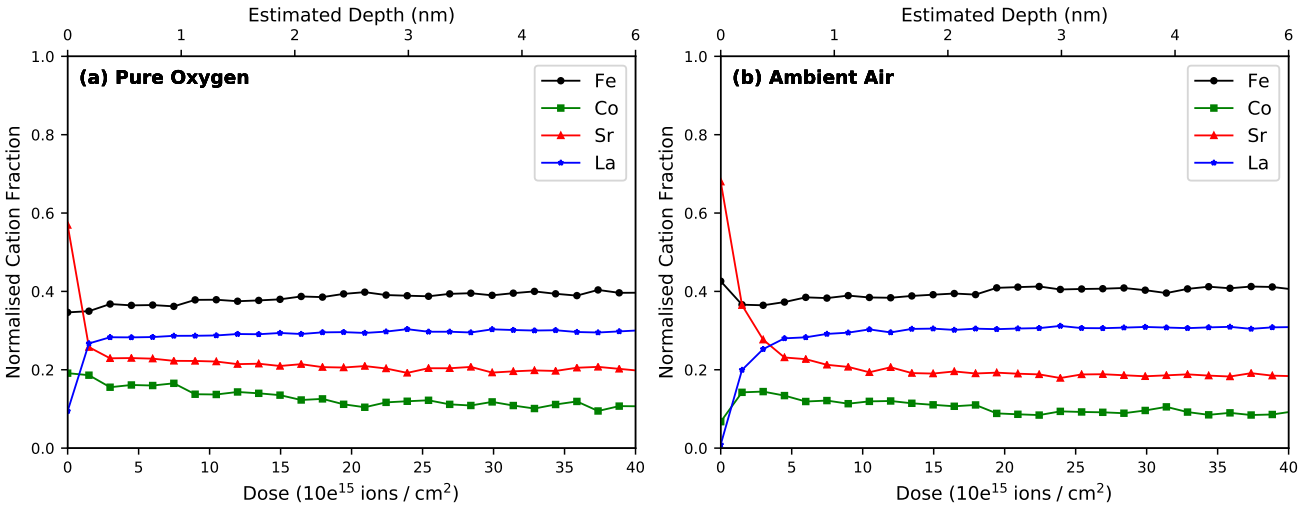


Fig. 13 5 kev Neon LEIS depth profiles of a sample showing the cation fractions for (a) annealed in pure oxygen and (b) in ambient air. The cation fractions have been normalised to bulk values and for clarity the total number of cations has been normalised to 1.

unusual. The LEIS data shows that strontium segregates to the surface even if particles cannot be observed, thus it is suggested that a strontium-based 'monolayer' is formed at the surface prior to and as part of the process of particle growth. From each atmosphere we can observe the following:

- **Oxygen:** In O_2 the predominant particle composition will be SrO (or potentially SrO_2 [32]). SrO is stable in air above 800 °C[33] which agrees with the observed onset of particle growth at 850 °C. Interestingly, particle growth is not linear as can be seen from Figure 1(a). The change in particle growth rate may be partly explained by the fact that the HT-ESEM images are a 2D representation of a 3D system and the height of the particles out the image plane cannot be readily determined.

- **Water:** In a pure H_2O atmosphere it may be suggested that $Sr(OH)_2$ particles might form, however, the stability of $Sr(OH)_2$ in air is approximately 400 °C. The smaller, darker particles are seen to grow first at 820 °C. These particles appear darker in the backscattered electron image and thus have a lower mass than the larger particles, therefore it is suggested that SrO particles are seen forming first. The larger particles appear to have a different chemical composition, however, the difference was not possible to determine. Both particle growth and surface coverage were significantly greater than in the other environments, suggesting that the processes governing particle agglomeration are more facile in the presence of water vapour.

- **Ambient air:** In air both H_2O and CO_2 are present (as well as contaminants like SO_x and NO_x), thus both $Sr(OH)_2$ and $SrCO_3$ may form at temperatures below 800 °C. The onset of particle growth is seen to be 950 °C, however, particle growth is very similar to that seen in pure oxygen. Given no particles form before 800 °C it is likely that only SrO particles are forming in this atmosphere and thus similar behavior is observed between growth in pure oxygen and ambient lab air. The delayed onset of growth may be explained by the formation of a passivating monolayer, possibly $SrCO_3$, and the time it would take to decompose this layer to allow the formation of the SrO particles.

4.1 Variation of the surface composition of the grains

AES was performed on the samples exposed to each environment in the HT-ESEM. The surface composition of the exposed grains determined by AES was consistent after annealing in each environment, however, the information depth of the AES technique is up to several nanometers and thus contains information from immediate surface and sub-surface layers. On the other hand LEIS is very sensitive to the outermost atomic layer. The LEIS results suggests that the immediate surface contains a larger proportion of strontium when the sample was annealed with a supplementary step in ambient air. It is also clear from the HT-ESEM result in pure water that strontium segregation, particle growth and agglomeration are significantly enhanced.

In ambient air the onset temperature of particle formation is higher than that of the other atmospheres. Sulphate particles have been observed on the surface of other MIEC materials[34], thus it is suggested that the basic hydroxide will react with acidic gases such as CO_2, SO_x and NO_x. The products of these reactions would appear to passivate the surface and prevent further particle growth.

4.2 Effect of the grain orientation

AES showed that the chemical composition of the grain surface was equal in each atmosphere, therefore, variations in particle growth must be due to the surface microstructure. In each environment particle growth is first observed at the grain boundaries. It is known that the diffusion of strontium is enhanced within grain boundaries in the related perovskite material $La_{0.6}Sr_{0.4}$-

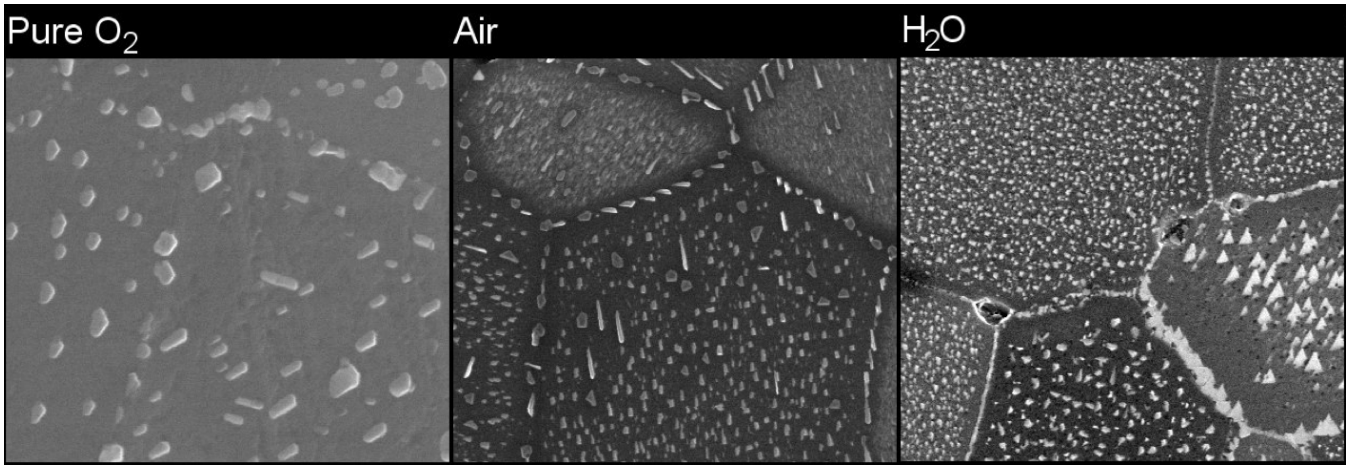


Fig. 14 Showing the clear difference in overall particle growth patterns of each atmosphere. The micrographs for oxygen and air were taken at the end of the experiment. In order to oberserve particles, the micrograph for the sample annealed in water has been taken at approximately 950 °C, prior to any significant particle agglomeration.

$CoO_{3-\delta}$ [35], however, it was also observed in all cases that particles grow within the body of the grains. As can be seen in Figure 14(H_2O) one grain (grain A from Figure 3(g)) has particles aligned along a common direction with a pyramidal shape. SrO has a cubic crystal structure therefore it is suggested that, at this grain orientation, the particles exhibit epitaxial growth orientated such that cubic growth appears pyramidal. The fact that not all grain orientation exhibits epitaxial growth could not be explained. As seen in Figure 14(Air), some grains exhibit a common growth direction, however, the particles were beyond the resolution of the experiment and a crystallographic relationship could not be determined. Interestingly, it was possible to observe particles that had grown orthogonal to the prevalent growth direction, suggesting that the underlying microstructure contains orthogonal features or that multiple particle compositions (with differing preferable epitaxial growth orientations) are formed at the surface.

Consistent with the literature twinning was observed in many of the grains using the forescattered electron imaging[36] and, as shown in Figure 15(a - b), particle growth in some grains (such as grain A from Figure 3) appear to exhibited a relationship with the twin planes whereby the particles appear to have the same orientation and are located predominantly along the twin habit plane direction. However, as shown in Figure 15(c - d), other grains (such as grain C from Figure 3) observed a twin structure but there is no obvious patterning of the particles on these grains. From the EBSD grain orientation maps we can see that these grains are orientated differently, however, due to the pseudo-symmetry problem, the absolute grain/twin orientation could not be uniquely determined.

On the other hand, a recent work[37] showed that on $La_{0.6}Sr_{0.4}CoO_{3-\delta}$ pellets (which showed greater symmetry and clearer EBSD analysis of crystal orientations) the {001} grain orientation had a higher area coverage of segregated SrO_x particles as compared to the {101} and {111}. A similar relation might hold for LSCF, however, solving the pseudo-symmetry problem is first required to assess this.

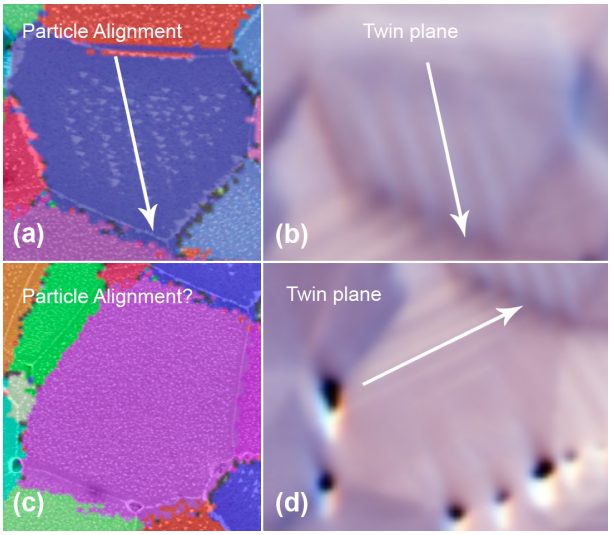


Fig. 15 Showing (a) aligned particle growth along equidistant parallel lines within grain A from Figure 3, (b) the Argus FSE image of the same grain showing twinning within grain A in the same direction as the particle growth, (c) homogeneous particle growth in grain C from Figure 3 at a different crystal orientation and (d) twinning within grain C.

It is still unknown what mechanisms are occurring at the surface, however, it is clear that at certain crystal orientations the presence of twins affects surface properties. The results presented in this work suggest that twinning either: (a) enhances diffusion rates within the domain structure[38] or (b) that the termination of the domain walls acts as heterogeneous nucleation sites.

4.3 Effect of the presence of surface defects

It was also observed that defects induced by polishing affected the growth of particles. In the case of the sample annealed in oxygen, this can be seen in Figure 16 by directional particle growth spanning multiple grains. Mechanical damage often forms dislocation networks within the bulk of the material. It is common for dislocation networks to exhibit enhanced transport properties[39].

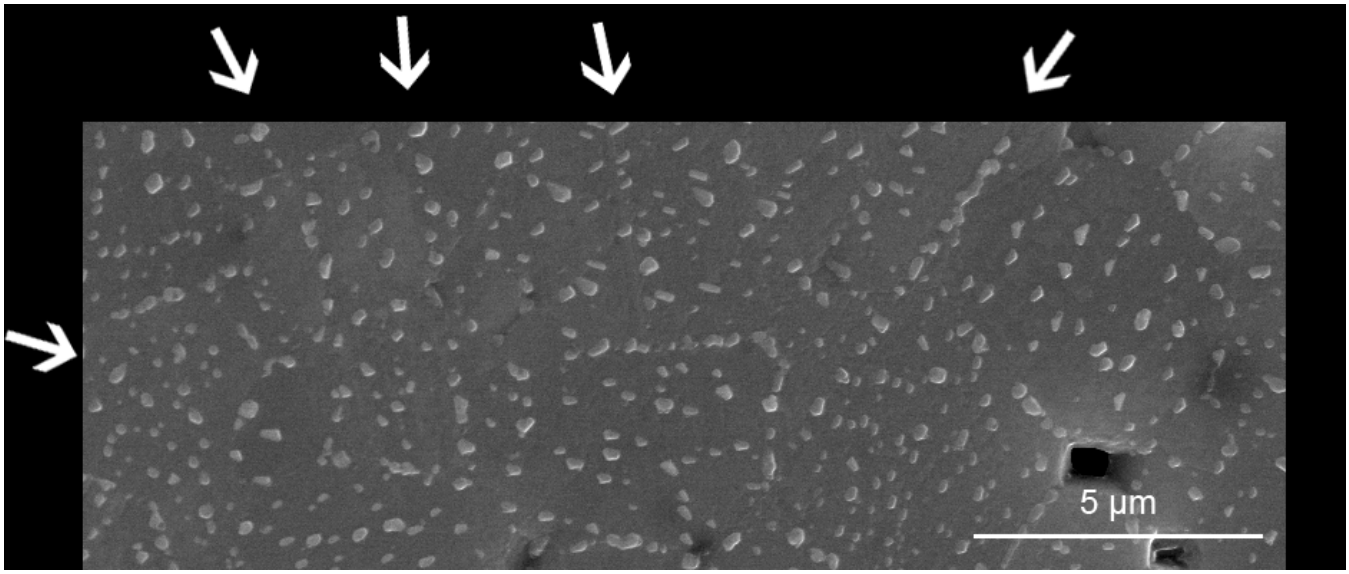


Fig. 16 Evidence for polishing induced mechanical damage as seen after the 1 hour isotherm at 1000 °C where (a) with particle growth seen on scratches in the sample annealed in pure oxygen and (b) a scratch without particle growth seen on the sample annealed in a low p(O_2) environment.

There is still dispute over the effect of a strained lattice on the diffusivity of anions and cations[40], however, this result also suggests that either there is enhanced segregation within the dislocation network or that the damaged surface acts as a heterogeneous nucleation site for the particles.

4.4 Proposed mechanism of precipitate formation

The mechanisms for particle growth have yet to be fully defined in the literature, however, it is clear from the data presented in this work that both the gas phase and the underlying microstructure influence the process of particle growth. Whilst a definitive description cannot be obtained as of yet, the following process for particle formation may be suggested (see Figure 17):

1. Strontium segregates to the exposed grain surface.
2. Once at the surface the strontium forms a monolayer as shown by LEIS data in this work and by Druce *et al.*[6].
3. Over time, sufficient strontium reaches the surface to form strontium-based particles as shown by Oh *et al.*[5] and the HT-ESEM data in this work.
4. Nucleation occurs initially at the grain boundaries as shown in the HT-ESEM data due to an increased strontium segregation rate (greater Sr^{2+} diffusivity)[35].
5. Mechanically induced defects may also act as heterogeneous nucleation sites.
6. Agglomeration occurs due to surface transport of the strontium.

This generalised process describes what was observed, however, specific mechanisms may be speculated from the data in this work and the literature. Strontium ions segregate as a reaction to a polar surface termination[8] and tend to form charge neutral Sr-O layers at the surface. Due to the presence of a strontium concentration gradient and other elements it is not strictly a 'monolayer' that forms, however, it may be considered analogous. As the surface coverage of Sr^{2+} species increase, it is believed that the monolayer begins to 'saturate' and forms SrO particles in order to compensate.

In oxygen the particle formation process should not deviate from the generalised process and it may be assumed that SrO or SrO_2[32] particles form directly. However, in the presence of water vapour and/or CO_2 the particle formation process is more complicated as the different gas species compete at the material surface. In ambient air the onset of particle growth and particle growth rate were greater than in O_2 and H_2O. It is known that these species affect the oxygen reduction reaction[41], however, this work also suggests that these species affect the rate of formation of Sr-based particles.

LEIS surface spectra has shown that, as anneal time and temperature increase, the only cation remaining at the surface is strontium, therefore, it may be assumed that a monolayer of a strontium-based phase is formed at the surface. In the presence of water, it has been proposed that chemisorbed hydroxyl groups sit on the surface of the material[13], therefore, segregating strontium will react to form $Sr(OH)_2$. In both oxygen and H_2O, particle growth was observed at approximately 850 °C. SrO is stable above 800 °C in air, therefore, it may be speculated that particle growth only occurs after the decomposition of $Sr(OH)_2$ into SrO:

$$Sr(OH)_2 \rightleftharpoons SrO + H_2O(g)$$

In an ambient air environment a similar observation was made, however it is suggested that the surface monolayer would be comprised of both $Sr(OH)_2$ and $SrCO_3$. In the presence of H_2O and CO_2, the $Sr(OH)_2$ phase is thermodynamically stable in air below 400 °C. From 400-800 °C the $Sr(CO)_3$ phase is the stable and above 800 °C the SrO phase is stable[33]. Therefore, above 800 °C,

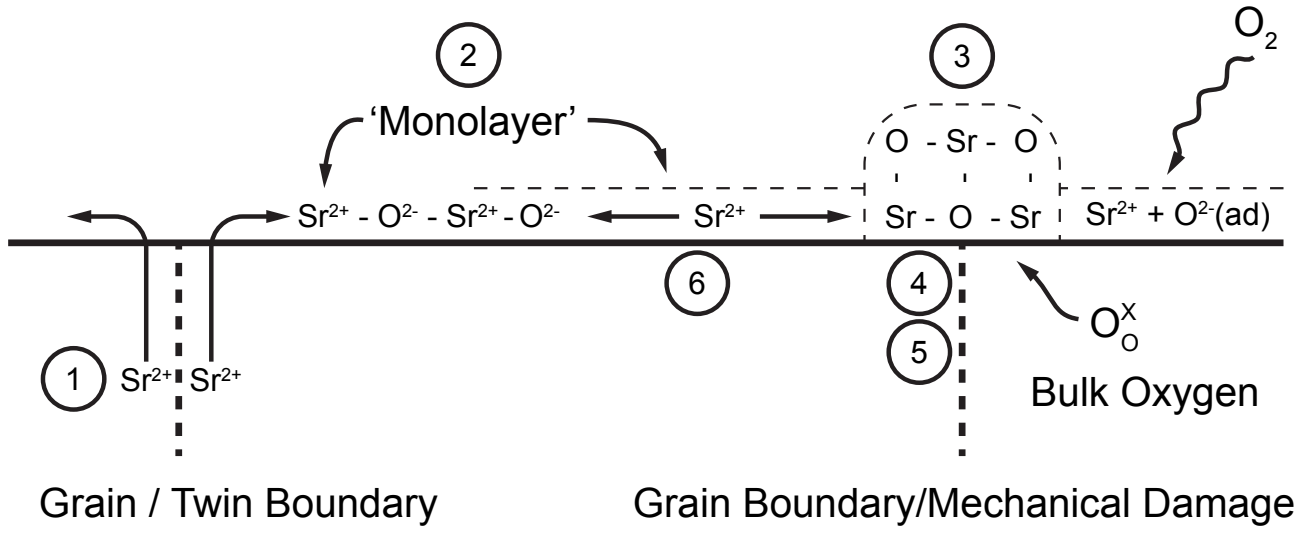


Fig. 17 Schematic of the proposed particle formation process.

a similar behaviour is observed where the phases comprising the monolayer decompose and form strontium based-particles.

5 Conclusions

HT-ESEM was performed to observe *in-situ* microstructural changes under three different atmospheres: pure oxygen, pure water and ambient air. In all atmospheres, particles were observed to grow on the surface of the sample but it was apparent that water had a much greater effect upon particle growth than the other atmospheres. The onset temperature and rate of growth varied between atmospheres, however, a number of common observations were made: (a) only strontium-based particles were observed, (b) particles were seen to grow both on the grain boundaries and the body of the grain, (c) defects such as scratches induced during polishing were preferable nucleation sites and (d) particles would agglomerate above a particular temperature in each atmosphere.

In the pure oxygen regime, particle growth occurred from 850 °C with a surface coverage of approximately 6%. Under pure water, particle growth was rapid from 850-1000 °C, reaching a maximum surface coverage of approximately 40-50%. Agglomeration occurs above 1000 °C and particles several microns along their longest length are formed. Agglomeration appears to be due to Ostwald ripening processes as denuded regions adjacent to the grain boundaries were wider in grains with a greater average particle size. Although the experiment was stopped after only a couple of hours, it would appear that the surface would eventually be covered completely by the agglomeration of the strontium-based particles. Under ambient air the onset of particle growth did not occur until 950 °C and was seen to cover approximately 10% of the surface. The delayed growth was attributed to the gradual decomposition of $Sr(OH)_2$ and $SrCO_3$ formed due to presence of CO_2 and H_2O.

EBSD was performed to assess the effect that the underlying microstructure had upon particle growth. It was observed that grain orientation affected particle growth. Certain grain orientations exhibited greater particle density than others. Due to the pseudo-symmetry problem LSCF exhibits, precise grain orientation could not be determined. In the grains exhibiting a relationship between particle growth and the underlying microstructure, it is suggested that observed super-structures such as twin boundaries act as either (a) fast diffusion pathways or (b) heterogeneous nucleation sites.

The observed changes in the modes of particle formation have prompted us to make a more detailed study into the interaction of the reactive constituents of air with SrO type segregated surfaces. These are being undertaken using Density Functional Theory (DFT) to investigate the interaction between this type of surface and H_2O molecules, O_2 molecules and CO_2 molecules and combinations of these species, as found in ambient air. This work will be the basis of a separate publication.

Conflicts of interest

There are no conflicts to declare.

Acknowledgements

This work was funded by the United Kingdom Engineering and Physical Sciences Research Council (EPSRC) under the grant number: EP/J003085/1.

Notes and references

1 R. Liu, S. Kim, S. Taniguchi, T. Oshima, Y. Shiratori, K. Ito and K. Sasaki, **196**, 7090–7096.
2 M. Yang, E. Bucher and W. Sitte, **196**, 7313–7317.
3 E. Bucher, C. Gspan, F. Hofer and W. Sitte, **238**, 15–23.
4 E. Bucher, C. Gspan, F. Hofer and W. Sitte, **230**, 7–11.
5 D. Oh, D. Gostovic and E. D. Wachsman, **27**, 1992–1999.
6 J. Druce, H. Téllez, M. Burriel, M. D. Sharp, L. J. Fawcett, S. N. Cook, D. S. McPhail, T. Ishihara, H. H. Brongersma and J. A. Kilner, **7**, 3593–3599.
7 Y. Orikasa, E. J. Crumlin, S. Sako, K. Amezawa, T. Uruga,

M. D. Biegalski, H. M. Christen, Y. Uchimoto and Y. Shao-Horn, **3**, F23–F26.
8 W. A. Harrison, **83**, year.
9 W. Lee, J. W. Han, Y. Chen, Z. Cai and B. Yildiz, **135**, 7909–7925.
10 Y. L. Huang, C. Pellegrinelli and E. D. Wachsman, **163**, F171–F182.
11 N. Sakai, K. Yamaji, T. Horita, Y. P. Xiong, H. Kishimoto and H. Yokokawa, **150**, A689.
12 S. J. Cooper, M. Niania, F. Hoffmann and J. A. Kilner, **19**, 12199–12205.
13 P. Hjalmarsson, M. Søgaard and M. Mogensen, **179**, 1422–1426.
14 W. Araki, M. Miyashita and Y. Arai, **290**, 18–23.
15 P. Vullum, H. Lein, M.-A. Einarsrud, T. Grande and R. Holmestad, **88**, 1187–1208.
16 Y. Kimura, K. Yashiro, S.-i. Hashimoto and T. Kawada, **161**, F3079–F3083.
17 B. Huang, R. Steinbrech and J. Malzbender, **228**, 32–36.
18 R. Podor, D. Pailhon, J. Ravaux and H.-P. Brau, **21**, 307–312.
19 D. Stokes, *Principles and Practice of Variable Pressure/Environmental Scanning Electron Microscopy (VP-ESEM)*, Wiley.
20 D. G. Lowe, **60**, 91–110.
21 I. Arganda-Carreras, V. Kaynig, C. Rueden, K. W. Eliceiri, J. Schindelin, A. Cardona and H. Sebastian Seung, **33**, 2424–2426.
22 M. D. Abràmoff, P. J. Magalhães and S. J. Ram, 7.
23 J. Canny, 20.
24 H. Brongersma, M. Draxler, M. Deridder and P. Bauer, **62**, 63–109.
25 X. Tan, N. Liu, B. Meng, J. Sunarso, K. Zhang and S. Liu, **389**, 216–222.
26 L. Tai, **76**, 273–283.
27 L. Tai, **76**, 259–271.
28 W. Araki, T. Yamaguchi, Y. Arai and J. Malzbender, **268**, 1–6.
29 G. Nolze, A. Winkelmann and A. P. Boyle, **160**, 146–154.
30 A. M. Glazer, **31**, 756–762.
31 J. Kilner, B. Steele and L. Ilkov, **12**, 89–97.
32 Y. Chen, H. Téllez, M. Burriel, F. Yang, N. Tsvetkov, Z. Cai, D. W. McComb, J. A. Kilner and B. Yildiz, **27**, 5436–5450.
33 D. R. Glasson and M. A. Sheppard, **18**, 327–329.
34 A. Berenov, A. Atkinson, J. Kilner, M. Ananyev, V. Eremin, N. Porotnikova, A. Farlenkov, E. Kurumchin, H. Bouwmeester, E. Bucher and W. Sitte, **268**, 102–109.
35 M. Kubicek, G. M. Rupp, S. Huber, A. Penn, A. K. Opitz, J. Bernardi, M. Stöger-Pollach, H. Hutter and J. Fleig, **16**, 2715.
36 W. Araki and J. Malzbender, **33**, 805–812.
37 F. Pikin, R. Bliem and B. Yildiz, **6**, 14136–14145.
38 J. A. Kilner and Y. Li, 12.
39 E. Navickas, Y. Chen, Q. Lu, W. Wallisch, T. M. Huber, J. Bernardi, M. Stöger-Pollach, G. Friedbacher, H. Hutter, B. Yildiz and J. Fleig, **11**, 11475–11487.
40 G. F. Harrington, S. J. Skinner and J. A. Kilner, **101**, 1310–1322.
41 J. Nielsen, A. Hagen and Y. Liu, **181**, 517–524.